ACS APPLIED MATERIALS & INTERFACES

Research Article

www.acsami.org

Controlled Fabrication of Polypyrrole Surfaces with Overhang Structures by Colloidal Templating

Sabine Akerboom,[†] Sidharam P. Pujari,[‡] Ayse Turak,[§] and Marleen Kamperman*[,†]

[†]Physical Chemistry and Soft Matter, Wageningen University, Dreijenplein 6, 6703 HB Wageningen, The Netherlands

[‡]Laboratory of Organic Chemistry, Wageningen University, Dreijenplein 8, 6703 HB Wageningen, The Netherlands

[§]Department of Engineering, Physics McMaster University, 1280 Main Street West, Hamilton, Ontario L8S 4L7, Canada

Supporting Information

ABSTRACT: Here we present the fabrication of polypyrrole (PPy) surfaces with a controlled overhang structure. Regularly structured PPy films were produced using interfacial polymerization around a sacrificial crystalline colloidal monolayer at the air/water interface. The morphology of the final inverse colloidal PPy film is controlled by the amount of monomer, the monomer: oxidant ratio and polymerization time. The PPy films exhibit an overhang structure due to depth of particle immersion in the water phase. As a result of the overhang structure, the PPy films are made hydrophobic, although the material itself is hydrophilic. The apparent contact angle of water on the structured surfaces is 109.5°, which is in agreement with the predicted contact angle using the Cassie−Baxter equation for air-filled cavities. This fabrication technique is scalable and can be readily extended to other systems where controlled wettability is required.

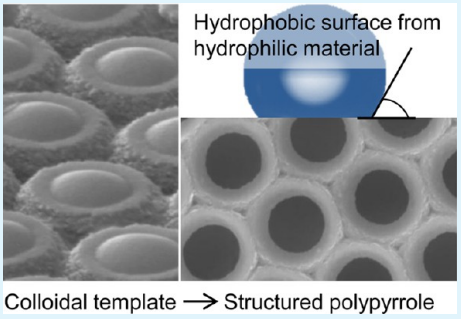

KEYWORDS: *polypyrrole, wetting, colloidal templating, interfaces, overhang structure, Cassie−Baxter model*

INTRODUCTION

Conducting polymers are an interesting class of materials because of the combination of traditional polymer properties with novel optical and electronic behavior.[1] They can be used in electronic nanodevices,[2−6] as chemical[7−10] or optical sensors,[11,12] in catalysis,[13] and energy storage.[14] A key parameter in many applications is the control of surface wetting. Hydrophobized conducting materials may be useful for corrosion protection, antistatics and conductive textiles.[15] One common method to induce hydrophobicity is to chemically change the surface energy. In the specific case of polypyrrole (PPy), chemical modification has been performed by copolymerizing pyrrole with a modified fluorinated pyrrole monomer,[16] adding different hydrophobic codopants,[17−20] or silanization of PPy.[21,22]

Alternatively, wetting properties can be changed upon structuring the surface.[23,24] In this way, the chemical composition is unaltered and the intrinsic electronic and optical properties of the PPy will be conserved. When pyrrole is polymerized, it usually grows in uncontrollable globules[25] and becomes a highly cross-linked, insoluble powder. The cross-linked nature makes PPy difficult to process.[26] One of the few reports on structuring PPy after synthesis uses laser patterning;[27] however, complex 3D structures cannot be fabricated in this way. A bottom up approach with the desired surface structure fabricated in situ during PPy synthesis is therefore highly desirable. This can be accomplished either by electrochemical or chemical synthesis. During electrochemical synthesis, pyrrole is polymerized to PPy at the anode. By changing the conditions, different structures can be fabricated,[6,28] including hollow microhorn arrays,[29] butterfly scale-like ordered porous structures,[30] 2D honeycomb structures,[31] and nanopillars.[32] Methods to chemically synthesize structured PPy films and coatings include interfacial synthesis at the water/organic solvent interface,[33−35] oxidant assisted synthesis,[36] and the use of templates. Both soft templates, consisting of surfactants,[37−39] and hard templates, consisting of colloids, have been employed to synthesize coated microspheres[40−44] and nanocups.[45]

As PPy is a hydrophilic material, structuring the surface by simply increasing the roughness of the PPy surface is likely to result in complete contact between the water and the solid surface under the droplet, also called the Wenzel state. The apparent contact angle in the Wenzel state (θ_w) is related to the roughness r of the material as[46]

$$\cos\theta_w = r\cos\theta \quad (1)$$

with θ the contact angle of the droplet on a perfectly flat substrate, and r the roughness of the surface (true contact area/projected area). The Wenzel state always magnifies the underlying wetting properties: the apparent contact angle for hydrophilic materials decreases, and the apparent contact angle for hydrophobic materials increases.[47] As the Wenzel equation therefore cannot be used to predict an increase in contact angle due to structuring of a hydrophilic material, the Cassie−Baxter

Received: May 5, 2015
Accepted: July 7, 2015
Published: July 7, 2015

DOI: 10.1021/acsami.5b03903
ACS Appl. Mater. Interfaces 2015, 7, 16507−16517

state is defined to describe this regime. In the Cassie−Baxter state, air is trapped underneath a droplet. The presence of air (which has a contact angle of 180° with water) effectively lowers the average surface energy,[48,49] which can yield hydrophobic apparent contact angles on intrinsically hydrophilic materials (θ < 90°). The apparent contact angle for a Cassie−Baxter state, $\theta_{CB,}$ is given by[50]

$$\cos\theta_{CB} = \varphi_s\cos\theta - (1 - \varphi_s) \quad (2)$$

with φ_s the fraction of the droplet that is in contact with the solid and $(1 - \varphi_s)$ the fraction of the droplet in contact with air.

However, for hydrophilic materials (θ < 90°) the Wenzel state is energetically more favorable. Therefore, to achieve hydrophobic behavior on hydrophilic materials, an energy barrier is required to maintain the Cassie−Baxter state.[22] For a surface containing cavities, this barrier can be provided by capillary forces that prevent water from entering these cavities.

This condition is met when the cavity has an overhang structure; in other words, the overhang angle, $\theta_{overhang}$, is smaller than the contact angle θ of water on a flat substrate.[22] Figure 1

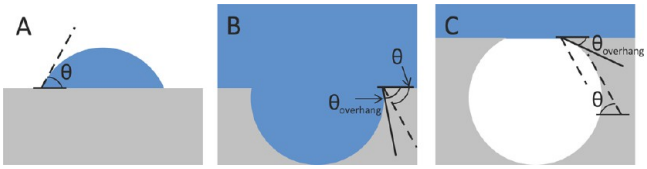

Figure 1. (A) Contact angle θ of water on a smooth substrate. This angle is denoted with a dashed line in A−C. (B) $\theta_{overhang}$ (solid line) > θ (dashed line): the droplet will wet the cavity. (C) $\theta_{overhang}$ (solid line) < θ (dashed line); the air/water interface needs to enlarge to wet the cavity which is energetically unfavorable.

shows this behavior for spherical cavities. If $\theta_{overhang} > \theta$, the inside of the cavity is readily wetted and the cavity fills with water (Figure 1B). When $\theta_{overhang} < \theta$, the air/water interface has to increase to reach the equilibrium contact angle θ (Figure 1C). The energy cost of creating this additional interfacial area is not compensated by the energy gain of the water wetting the hydrophilic walls and the droplet will thus not enter the cavity.[51]

In this paper, we use a colloidal template to create PPy surfaces with overhang structures. The colloidal template consists of a monolayer of polystyrene (PS) particles at the air/water interface with PPy grown at the particle/water interface. To obtain overhang structures, colloidal particles that are hydrophilic, and hence deeply immersed in the water phase, are used. We systematically study the different morphologies that can be fabricated using this method, and show that the surface switches from hydrophilic to hydrophobic upon structuring.

EXPERIMENTAL SECTION

Materials. All materials were purchased from Sigma-Aldrich and used as received.

Particle Synthesis. Carboxylated PS particles were synthesized in a one-step synthesis according to ref 52. Briefly, Milli-Q water (120 g), itaconic acid (0.5 g) and styrene (24.5 g) were heated to 80 °C in a round-bottom flask, and flushed with nitrogen for 45 min. Meanwhile, 4,4′-azobis(4-cyanovaleric acid) (252.4 mg) was dissolved in 1 M NaOH (2 g): water (6.3 g) solution. After adding this solution to the round-bottom flask, the mixture was reacted overnight under continuous stirring at 500 rpm. The product was filtered over glass wool to discard waste coagulum that formed during the reaction, and was washed in water by three cycles of centrifugation at 4500 rpm for 1 h followed by resuspension in Milli-Q water. After this washing step, the colloids were exchanged to ethanol, and washed three times in ethanol following the same procedure. Using static light scattering, the radius of the particle, R_p was found to be 574 nm, and the polydispersity index (PDI) (R_w/R_n) was 1.01. The parking area (particle surface area)/(number of charges per particle), was determined using titration and found to be 0.11 nm^2 per charge.[53]

Flat PPy Surfaces. Flat PPy surfaces were prepared according to ref 54. Briefly, microscope slides were submerged in KOH (5 M) for 30 min and thoroughly rinsed with water. Water (10 mL), ethanol (90 mL) and (3-aminopropyl)triethoxysilane (APTES, 100 μL) were mixed and stirred for 2h to hydrolyze the APTES. The microscope slides were subsequently submerged in hydrolyzed APTES solution for 6 h. After this, the microscope slides were rinsed with ultrapure water and put under vacuum at RT overnight. The contact angle changed from <5° (after KOH treatment) to 52.2° ± 0.6° after APTES treatment, which is consistent with the initial contact angle found for APTES monolayers.[55] The dried microscope slides were placed diagonally in a 50 mL beaker, containing a 36 mM aqueous solution of $FeCl_3$ (40 mL). Pyrrole (100 μL) was added and the reaction was allowed to proceed for 8 h under gentle stirring. PPy aggregates were removed from the surface with a tissue and by using excessive rinsing.

Characterization. *Scanning Electron Microscopy (SEM).* Samples were prepared by scooping part of the floating monolayer from the air/water interface using cut silicon wafers as substrate. To prevent self-folding upon drying, Leitsilber 200 Silver Paint (Ted Pella) was used to glue the films to the substrate. Samples were sputtered with gold (30 mA, 40s) using a JEOL JFC-1300 autofine coater, and imaged using a JEOL JAMP-9500F field-emission Auger microprobe at 10 kV.

X-ray Photoelectron Spectroscopy (XPS). XPS spectra were measured on a JPS-9200 X-ray photoelectron spectrometer (JEOL, Japan). High resolution spectra were obtained under UHV conditions using monochromatic Al Kα X-ray radiation at an angle of 80° at 12 kV and 20 mA, using an analyzer pass energy of 10 eV. Spectra were corrected with a standard background subtraction according to a linear procedure before fitting. The spectra were fitted using Casa XPS software (version 2.3.15) and to compensate for the surface charging effects, the N 1s peak was calibrated at a binding energy of 399.6 eV, in accordance with ref 56. Calculated atomic percentages were normalized by the corresponding atomic sensitivity factors.

Energy-Dispersive Spectroscopy (EDS). Samples were first imaged at 2 kV, 6 pA, at room temperature, in a field-emission scanning electron microscope (Magellan 400, FEI, Eindhoven, The Netherlands). EDS analyses were accomplished by an Oxford X-max detector and analysis software (Oxford Instruments Analytical, High Wycombe, England) at an acceleration voltage of 10 kV, 0.8 nA.

Contact Angle Measurements. Contact angles were determined using the Kruss Contact Angle measuring System G10 and using the "Drop Shape Analysis" software. Samples consisted of PPy films mounted on a coverslip using double sided tape and left to dry for at least a week at RT. Contact angles were measured on at least 5 locations using droplets of 5 μL.

RESULTS AND DISCUSSION

3.1. Fabrication and Characterization of PPy-Inverse Crystalline Colloidal Monolayers. *3.1.1. Surface Structure Fabrication.* The fabrication process of PPy inverse colloidal monolayers (PPy-iccm) is shown in Scheme 1. First, a crystalline colloidal monolayer is prepared using carboxylated PS particles as described in ref 53 (Scheme 1A). These carboxylated PS particles (d = 1.15 μm) are selected because the carboxylic acid surface groups (1) allow control over the PS particle ordering by pH, and (2) make the particles hydrophilic, ensuring high immersion depths in the subphase (i.e., water underneath the particles).

The monolayers are prepared in PS Petri dishes (typical diameter 50 mm) filled with water at pH 8−10, and ionic strength of 1×10^{-1} to 1×10^{-3} M (unless stated otherwise). A dispersion of particles in ethanol is applied to the air/water

DOI: 10.1021/acsami.5b03903
ACS Appl. Mater. Interfaces 2015, 7, 16507−16517

Scheme 1. Schematic Representation of the Preparation of PPy Inverse Crystalline Colloidal Monolayers[a]

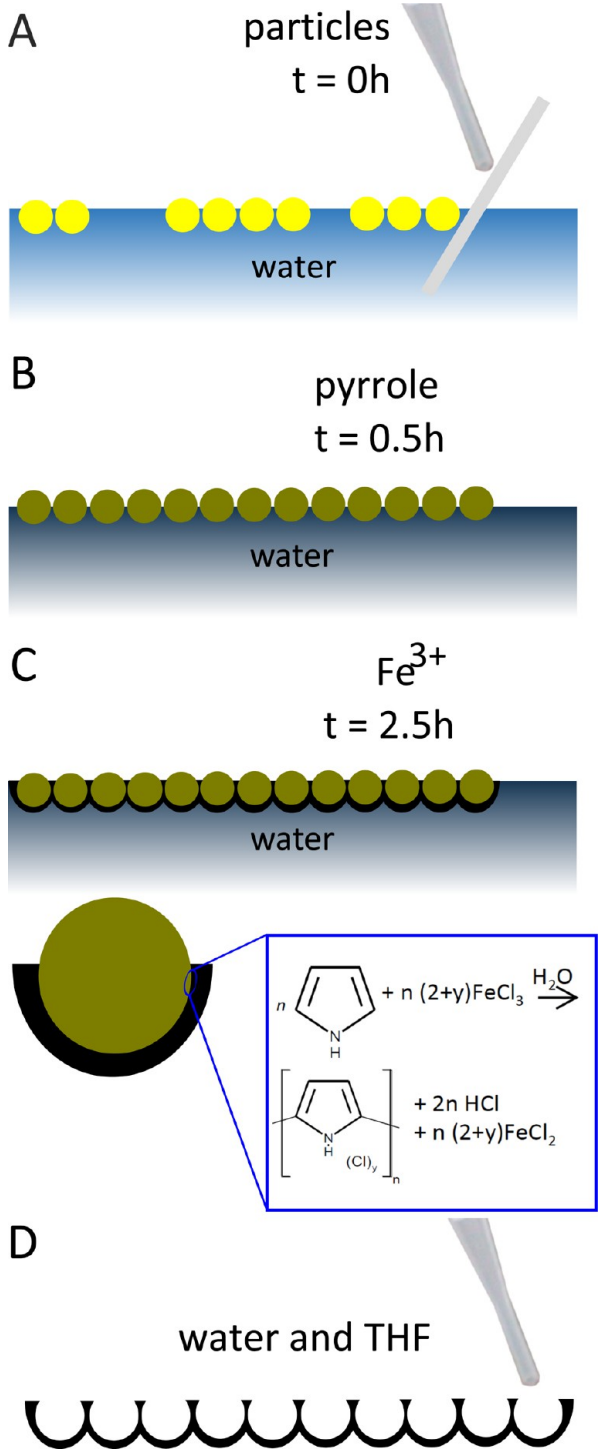

[a](A) Monodisperse carboxylated PS particles are applied to the air/water interface; (B) Pyrrole is added to the subphase; (C) Fe^{3+} is added to the subphase and interfacial polymerization of pyrrole starts; (D) Film is washed with water and PS particles are removed with THF.

interface via a piranha-cleaned coverslip using a pipet. The samples are left to equilibrate for at least 30 min to ensure evaporation or dissolution of all ethanol.

Second, pyrrole is added to the subphase (Scheme 1B). Pyrrole either remains as a droplet on the bottom of the Petri dish, or forms a ring at the air/water/Petri dish contact line. Since pyrrole is more soluble in PS than in water, these monomers diffuse into the PS particles. Each particle thus acts as a reservoir for monomers, as has also been observed for aniline.[57,58]

Third, 2 h after pyrrole addition, a 1 M solution of ferric chloride is added to start the interfacial polymerization (Scheme 1C). As polymerization occurs only where Fe^{3+} and pyrrole are present, the reaction is limited to the PPy/water interface.[59] The ferric chloride in the water can either oxidize a pyrrole monomer directly,[60] or first act as a Lewis acid, after which an electron from the aromatic ring can more easily be taken, resulting in an oxidized pyrrole monomer.[61] Next, the radical cation reacts either with another monomer, after which oxidation and deprotonation results in a dimer or it reacts with another oxidized monomer.[60] This dimer can be oxidized again, and hereafter attack another monomer, thus driving the polymerization. Pyrrole monomers are supplied by diffusion of the monomers through the PS and PPy matrix to the polymer/water interface. The reaction is allowed to proceed for at least 24 h to ensure complete conversion.[62] This step is especially important for samples with low amounts of pyrrole or Fe^{3+}. The lid of the Petri dish is closed during this time, to prevent pyrrole evaporation.[61]

During pyrrole polymerization, the color of the samples changes from yellow/orange (from Fe^{3+}) to black. This color change happens within a minute when a high amount of pyrrole and a high Fe^{3+}:Py ratio are used, but can take hours for lower amounts of pyrrole and low Fe^{3+}:Py ratio. No color change is observed within 24 h when no ferric chloride is added.

Fourth, after polymerization, PPy crystalline colloidal monolayers (PPy-ccm) are washed by removing the subphase using a syringe and replacing it with ultrapure water (Scheme 1D). This washing step is repeated three times. The monolayers are subsequently transferred by immersing the Petri dish in a large clean water bath, containing at least 250 mL water. As the monolayers float, they can be scooped up with another clean Petri dish. The particles are extracted from their PPy matrix by dissolving them in THF for at least 2 h, resulting in a PPy inverse crystalline colloidal monolayer (PPy-iccm). The PPy matrix is thick and stiff enough (Young's modulus of around 1 GPa)[63] to prevent collapse of the inverse colloidal structure. An example of a PPy-iccm is shown in Figure 2, and more examples can be found in Figure S1 in the Supporting Information.

3.1.2. Chemical Characterization of PPy-iccm. Wetting behavior is heavily influenced by the chemical composition of the

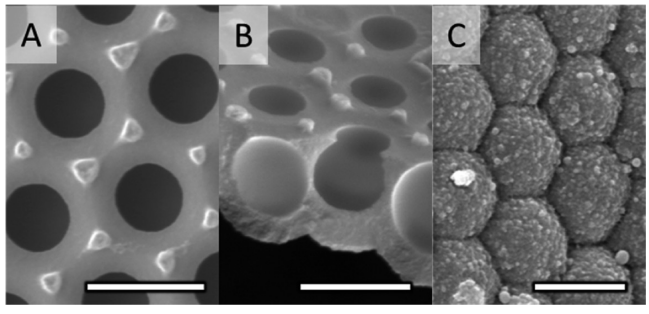

Figure 2. SEM micrographs of washed PPy surface structure (PPy-iccm) made with 2.1 μL Py cm^{-2} and a Fe^{3+}: Py ratio of 2.3 (mol/mol). (A) Top-surface (facing air during polymerization); (B) side view; (C) bottom-surface (facing water during polymerization). All scale bars represent 1 μm.

DOI: 10.1021/acsami.5b03903
ACS Appl. Mater. Interfaces 2015, 7, 16507−16517

system. To confirm that PPy was fully formed during iccm preparation, the elemental composition of the films was determined by XPS measurements and EDS measurements were performed to check for compositional variations within the film.

XPS Measurements. Elemental composition was determined with XPS measurements on a PPy-iccm sample synthesized with 2.1 μL Py cm^{-2} and Fe^{3+}:Py = 2.3, both at the top-surface of the sample (facing air during polymerization) and bottom-surface (facing water during polymerization). The XPS survey scan (Figure 3A, B) shows C and N as expected for pure PPy, as well as contaminants Cl, O and, at the bottom-surface, Fe. Core level peaks for C and N (see Figures S2 and S3 in the Supporting Information) are fitted and assigned as described in ref 59. The assigned peaks are listed in Figure 3C. The fitting procedure for C 1s and N 1s indicated that our iccm indeed consists of PPy (see S2 and S3 and further details in Supporting Information).

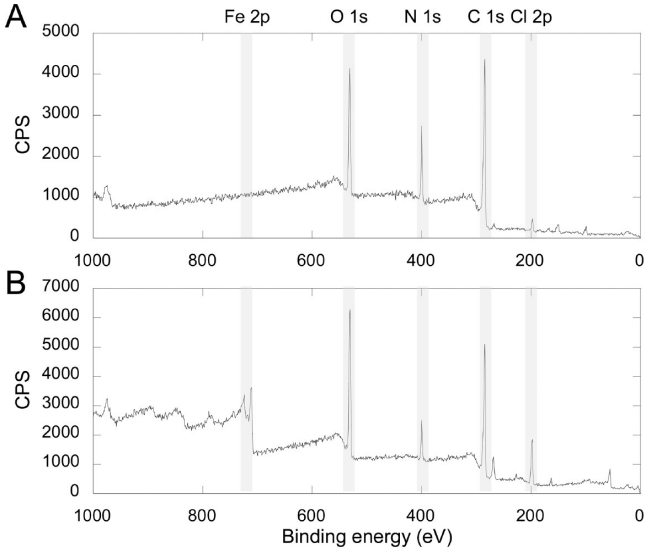

C

Element	Binding Energy (eV) ± 0.1eV	Bottom surface (%)		Top surface (%)	
		Survey scan	Core level peaks	Survey scan	Core level peaks
N 1s		7.6		12.8	
C=N	398.6		4.3		12
NH, N-pyrrol	399.6		36.5		80
C-N+	400.5		5.1		8
C=N+	401.4		6.1		--
Fe-N	396.4		50.8		--
O 1s		21.8		18.3	
Fe-O,			21.1		56
C=O			59.4		44
C-OH			19.5		--
C 1s		59.2		67	
C_{beta}	283.6		34		37.1
C_{alpha}	284.4		38.1		31.5
C-OH, C=N, C-N-	285.4		12.5		14.1
C=O, COOH, COO-	287.1 (Top) & 287.6 (Bottom)		15.4		17.3
Fe 2p3/2	710.9	3.6	100	--	--
Cl 1s	163.5	7.8	100	1.8	100

Figure 3. (A) XPS survey scan of the PPy-iccm top-surface; (B) XPS survey scan of the PPy-iccm bottom-surface; (C) table with all the relative XPS peaks for survey scan and curve fitting results for core level peaks.

On the basis of the reaction as presented in Scheme 1, only signals from N 1s and C 1s are expected. Assuming that all N originates from pyrrole (and thus neglecting any N from the initiator during particle synthesis) and that no N is cleaved off during side reactions, the percentage of C 1s alpha and beta signal that can be attributed to polypyrrole (one N is attached to 4 C, thus pure pyrrole is 5× N 1s) can be determined. These calculations indicate a lower amount of pyrrole at the bottom surface (38% vs 64% for the top-surface). The rest of the C 1s signal may be attributed to two additional processes: residue PS adsorption after particle dissolution and side reactions during pyrrole polymerization.

A common side reaction is overoxidation, which is the gradual oxidation of PPy by water in the presence of $FeCl_3$ and results in O incorporation in the polymer matrix.[41,42,58,64,65] Another common side reaction is the incorporation of dopants, such as chloride, that results in the Cl 2p signal from charge transfer interactions with the polymer backbone.[42] Other dopant species, i.e. iron(III) chlorides ($FeCl_4^-$, $FeCl_3$),[62] can only be found at the bottom-surface, since the Fe 2p signal is absent at the top-surface. Part of this Fe is coordinated to N, as evidenced by the N 1s core level spectrum for the bottom-surface (see Figure S3 in the Supporting Information). The pyrrole rings at the bottom-surface thus underwent further reactions while in contact with the $FeCl_3$ solution. Additional evidence for further reactions at the bottom-surface can be determined from the (NH, N-pyrrole):N═C ratio. For the bottom-surface we find a high ratio of 6.7, whereas this ratio is only 4.8 for the top-surface.

In addition to the presence of oxygen from overoxidation, O may stem from incomplete removal of the PS particles. The particles consist of copolymerized styrene (C_8H_8) and itaconic acid ($C_5H_6O_4$). The presence of polystyrene-*co*-poly(itaconic acid) residues is also indicated by the enrichment of the signal in C compared to N (N:C of 1:5.2 for the top-surface, and N:C of 1:7.8 for the bottom-surface).

EDS Measurements. In SEM micrographs of PPy-iccm (2.1 μL Py cm^{-2}, Fe^{3+}:Py = 2.3), triangular protrusions were observed at the top-surface that appear white in SEM (see Figure 2A, B). This contrast is either due to the surface topology or differences in chemical composition. EDS was performed to study compositional variations, and the maps can be found in Figure 4 (and the EDS spectra in Figure S6 in the Supporting Information). C and O are evenly distributed over the sample (Figure 4A, C), and no differences are found between the protrusions and the rest of the sample. There is almost no Fe found on the top-surface (Figure 4B), in agreement with the XPS data. In the overlay map Si is observed (indicated in red), which stems from the support material. The visible features in the SEM micrographs can thus be attributed solely to surface topology.

3.2. Control over Surface Morphology. *3.2.1. Control over Monolayer Crystallinity.* PPy-ccms were fabricated using colloidal monolayers prepared at the air/water interface using water at different pH values, i.e., pH 3, pH 5, and pH 10. The ionic strength was kept constant at 1 mM. The ordering of the particles during monolayer formation is governed by the competition between capillary attraction and electrostatic dipolar repulsion between the particles. This balance between attraction and repulsion can be controlled by the pH and ionic strength of the subphase.[53] At high pH, the carboxylic acid groups of the

DOI: 10.1021/acsami.5b03903
ACS Appl. Mater. Interfaces 2015, 7, 16507−16517

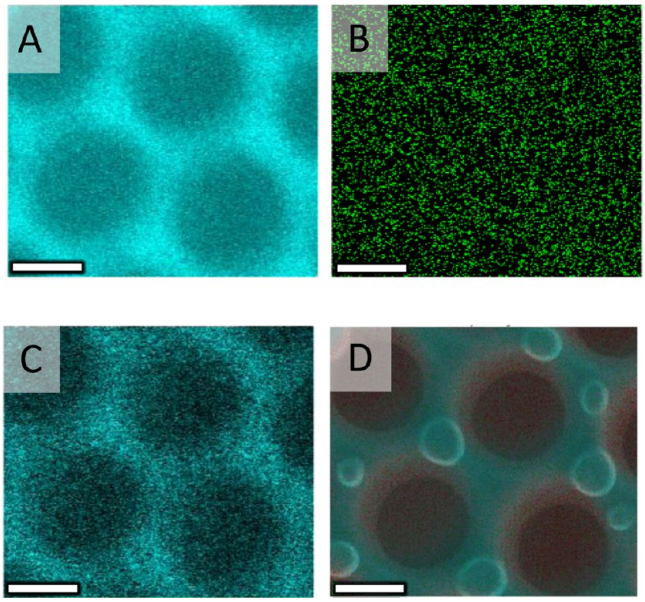

Figure 4. EDS maps of PPy-iccm (2.1 μL Py cm^{-2}, Fe^{3+}:Py = 2.3) for (A) C Kα, (B) Fe Kα, and (C) O Kα. (D) overlay map with C Kα (turquoise), Fe Kα (green), and Si Kα (red, from support material).

itaconic acid (with pK_{a1} = 3.85 and pK_{a2} = 5.44)[66] are deprotonated, giving rise to an increase in electrostatic repulsion. This increased electrostatic repulsion counteracts the attractive van der Waals and capillary forces. Consequently, the particles remain more mobile at the interface resulting in more ordered monolayers. This allows the particles to assemble in a hexagonal packing,[67] thus resulting in crystalline monolayers. At low pH, the carboxylic acid groups on the surface of the monomers are protonated, and hence no electrostatic repulsion between the particles exists. Particles that approach each other closely (i.e., by capillary forces) thus immediately feel the attractive van der Waals forces that bring them in close contact. This process immobilizes the particles and results in close-packed monolayers with relatively low crystallinities.

The final PPy-ccm structure prepared at pH 3, though close-packed, shows low crystallinity (Figure 5A), which is consistent with the poor order in the monolayer. The crystallinity of the monolayers prepared at neutral and high pH increases with increasing pH and is preserved in the PPy-ccm (Figure 5B, C), although both the pH and the ionic strength of the subphase change during polymerization. The ionic strength increases dramatically upon addition of the Fe^{3+}, and the pH drops during polymerization due to proton release (see Scheme 1C). Assuming complete conversion of pyrrole monomers, the theoretical pH value for this sample decreased to 1 during polymerization. Conserving the crystallinity is therefore surprising, as it has previously been observed that changing the pH after the preparation of the monolayer decreases the particle order.[53] The pyrrole here appears to act as a glue between the particles early in the polymerization process, preserving the crystallinity in the PPy-ccm layer.

3.2.2. Amount of Pyrrole. The samples in Figure 5 are made using 2.9 μL pyrrole per cm^2 of monolayer. The molar ratio Fe^{3+} to pyrrole is chosen to be 2.3, which is the same value as used in ref 68. Keeping this ratio and the crystallinity of the monolayer fixed, samples were prepared using different amounts of pyrrole ranging from 0.042 to 8.4 μL cm^{-2}. At the lowest amount of pyrrole, PPy-fibrils appear to be adsorbed on the PS particles

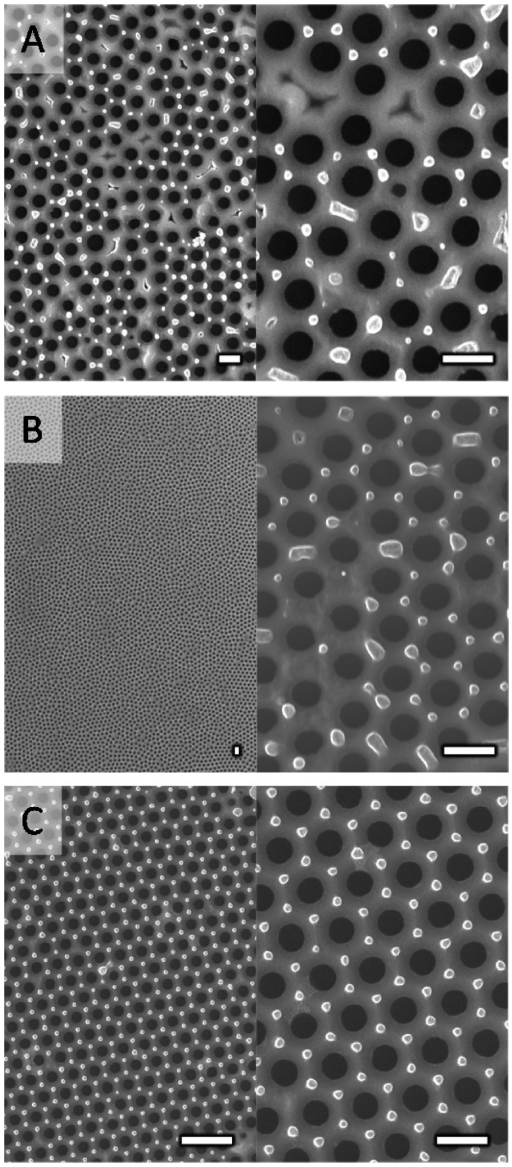

Figure 5. (A–C) Scanning electron micrographs showing the effect of subphase composition on PPy-ccm surface structure at fixed [Py] of 2.9 μL cm^{-2} and Fe^{3+}:Py ratio of 2.3 mol/mol. Subphases: (A) pH 3, [salt] = 1 mM; (B) ultrapure water; (C) pH 10, [salt] = 1 mM; all scale bars represent 1 μm.

(Figure 6A). Increasing the amount of pyrrole to 0.084 μL cm^{-2}, results in particles coated with a PPy layer (Figure 6B). This PPy layer thickens upon increasing the amount of pyrrole (Figure 6C), and at 0.42 μL pyrrole cm^{-2} the PPy forms a continuous layer with triangular dimples (Figure 6D). At even higher PPy concentrations, the edges of these triangular dimples protrude from the PPy surface (0.84 μL pyrrole cm^{-2}) (Figure 2E) and at 2.1 μL pyrrole cm^{-2} triangular protrusions are formed (Figure 6F). The final structure of the PPy-iccm can thus be varied by choosing the amount of pyrrole at fixed Fe^{3+}:Py molar ratio.

3.2.3. Molar Ratio Py:Fe. A similar effect can be obtained by varying the Fe^{3+}: Py molar ratio. Figure 7 shows the results of varying this ratio from 0.07 to 1.5 at a fixed amount of 0.42 μL pyrrole cm^{-2}. At the highest ratio, the final structure is a continuous PPy surface with triangular dimples (Figure 7D). However, at the lowest ratio, no traces of PPy are visible (Figure 7A). In between these extremes, PPy coatings on the PS particles

DOI: 10.1021/acsami.5b03903
ACS Appl. Mater. Interfaces 2015, 7, 16507–16517

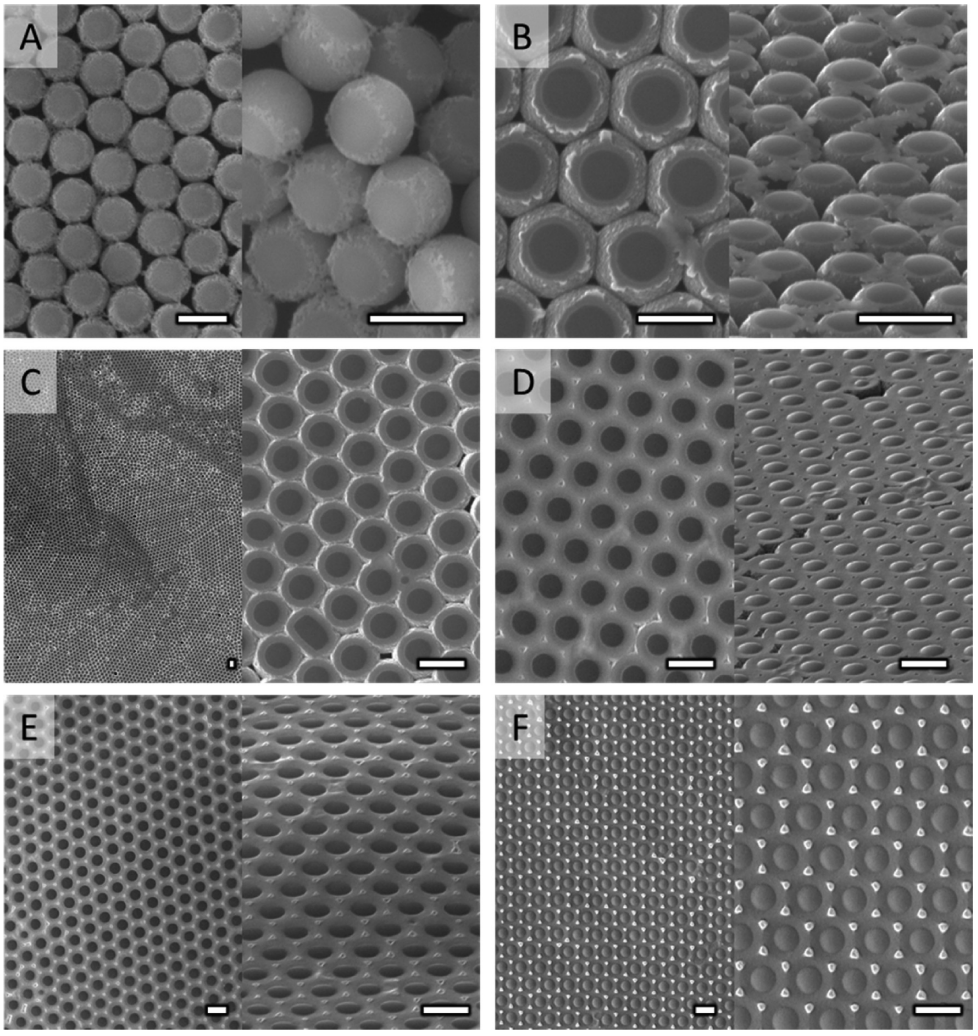

Figure 6. SEM micrographs showing the effect of amount of PPy on PPy surface structure at fixed Fe^{3+}: Py ratio of 2.3. Pyrrole (μL cm^{-2}) added: (A) 0.042, (B) 0.084, (C) 0.21, (D) 0.42, (E) 0.84, and (F) 2.1. All scale bars represent 1 μm.

were obtained that increased in thickness with increasing molar ratio (Figure 7B, C).

3.2.4. Morphology Diagram. The different PPy surface structures obtained for different amounts of pyrrole and Py: Fe ratios as determined from SEM micrographs can be divided in four classes: (1) PPy fibrils; (2) thin coating on the PS particles; (3) interconnecting PPy matrix with triangular dimples at the interstitial spaces; (4) interconnecting PPy matrix with triangular protrusions. These four classes are shown in a two-dimensional morphology diagram in Figure 8.

3.2.5. PPy Matrix Growth. Close inspection of the SEM micrographs of morphology class 4 (see for example Figure 2A, B) shows that the PPy top-surface (facing air during polymerization), is smooth. In most reports in the literature, PPy layers show a granular morphology.[69] In addition, we note that the PPy surface is not flat in between the particles, but rather, follows a positive slope radiating from the particle. The SEM image in Figure 2C shows the bottom-surface of the PPy-iccm. The PPy coating around the particles follows the outline of the particles, and the surface is rough.

To study how these features arise during interfacial polymerization, colloidal monolayers were swollen with 2.9 μL pyrrole cm^{-2} and investigated at different incubation times after adding the ferric chloride. The molar ratio of Fe^{3+}: Py was kept constant at 2.3. The first sample was taken immediately after ferric chloride addition (Scheme 2A) and shows that a thin, rough PPy layer on the outside of the immersed parts of the particles is directly synthesized. The layer around the particle thickens after longer incubation times (Scheme 2B), resulting in an interconnecting PPy matrix. The water present in the interstitial space of the particles at the top-surface, may thereby be cut off from the bulk water below. The PPy keeps growing at the rough water/PPy interface and while doing so, it is pushed upward, enabling the PPy to grow higher than the original water level (Scheme 2C). The smooth layer radiating from the particle is believed to originate from the air/water/PPy contact line, which slowly moves upward. Protrusions may arise because of polymer formation in the small remaining water droplet sitting at the interstitial sites (Scheme 2D).

The variation in surface structure with time is used to produce a PPy-ccm with a surface structure gradient. To this end, a colloidal crystal monolayer was prepared in a Petri dish with a diameter of 13.6 cm and 0.98 μL pyrrole cm^{-2} was added to the left side. Fe^{3+} in a molar ratio Fe^{3+}:Py of 2.6, was added after 15 min at the same location as where the pyrrole was added. Figure 9A shows a picture taken almost immediately after Fe^{3+} addition. The Fe^{3+} solution spread quickly: the subphase was completely yellow. However, only on the left side rapid polymerization of the

DOI: 10.1021/acsami.5b03903
ACS Appl. Mater. Interfaces 2015, 7, 16507−16517

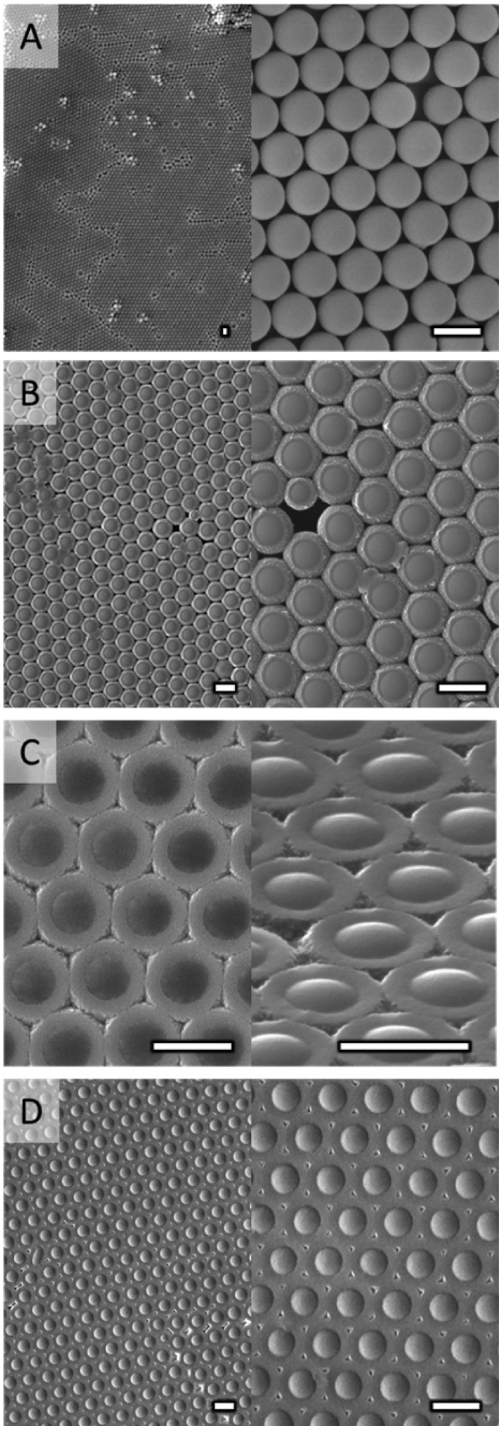

Figure 7. SEM micrographs showing the effect of Fe^{3+}: Py ratio on PPy surface structure at fixed [Py] of 0.42 of μL cm^{-2}. Fe^{3+}: Py ratio: (A) 0.07, (B) 0.33, (C) 0.72, and (D) 1.5. All scale bars represent 1 μm.

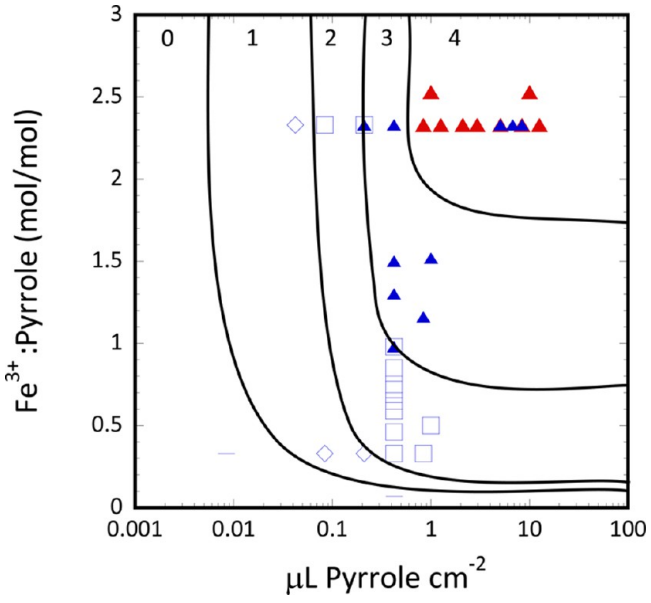

Figure 8. PPy surface morphology diagram. (0) blue dash, no PPy visible; (1) blue diamond, PPy fibrils; (2) blue square, PS particles coated with a PPy layer; (3) blue triangle, interconnecting PPy matrix with triangular dimples; (4) red triangle, interconnecting PPy matrix with triangular protrusions. Lines are added as guide to the eye.

Scheme 2. Growth of PPy in Time (not to scale) and SEM Micrographs[a]

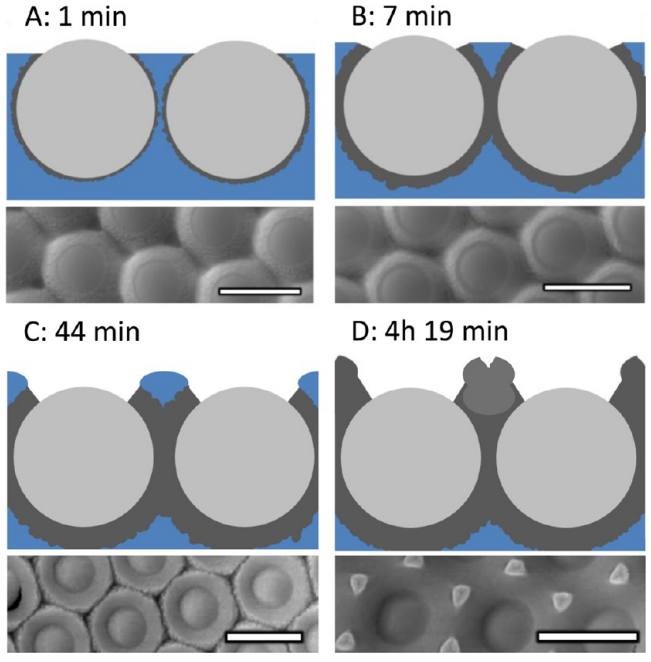

[a]SEM micrographs taken at (A) 1, (B) 7, and (C) 44 min, and (D) 4 h 19 min after Fe^{3+} addition. [Py] is 2.9 μL cm^{-2} and Fe^{3+}: Py ratio is 2.3 mol/mol. All scale bars represent 1 μm.

pyrrole was observed, as evidenced by the black color. The picture in Figure 9B shows the sample after 24 h, and it can be seen that the complete Petri dish is covered with a PPy-ccm.

Four samples were scooped from left to right using silicon wafers of around 1 cm^2. The PPy surface structures from the edges, denoted C and D, can be found in Figure 9C–D, the two samples from the middle in Figure S7 in the Supporting Information. The surface structure of the sample taken nearest to the location where pyrrole was added, location C, shows triangular protrusions (morphology class 4), whereas triangular dimples (morphology class 3) are found that grow in size as the sample is taken farther to the right.

3.3. Wetting of PPy. *3.3.1. Wetting of Flat and Structured PPy.* The contact angles of water on PPy-iccms with different morphologies (Class 2–4 from morphology diagram) were measured and were all found to be very similar: 109.5 ± 0.7° for PPy-iccm with triangular protrusions (Class 4), 109.2 ± 1.0° for

DOI: 10.1021/acsami.5b03903
ACS Appl. Mater. Interfaces 2015, 7, 16507–16517

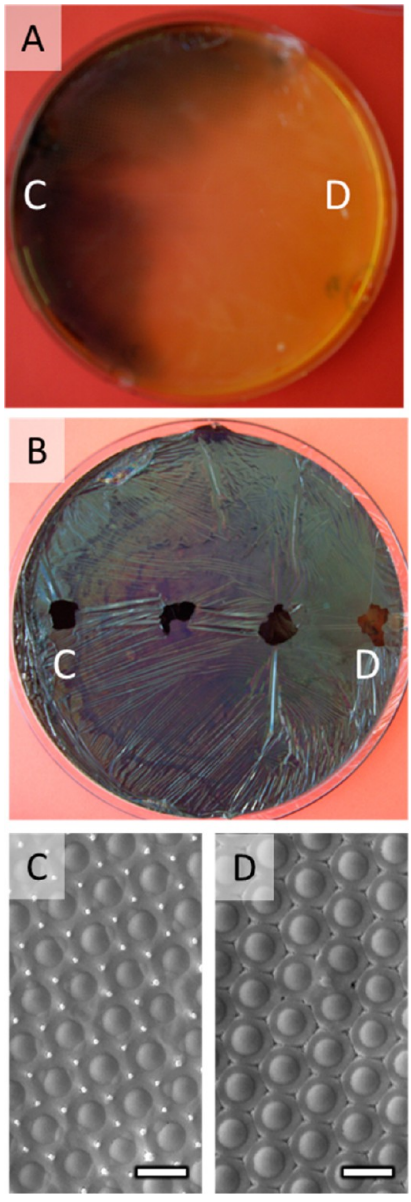

Figure 9. Gradient of PPy surface structures within one sample with 0.98 μL Py cm^{-2} and a Fe^{3+}: Py ratio of 2.6. (A) Sample shortly after Fe^{3+} addition. Pyrrole and Fe^{3+} were added on the left-hand side. (B) Sample after 24h. (C, D) Surface structures at different locations, as indicated in A and B. All scale bars represent 1 μm.

PPy-iccm with triangular dimples (Class 3) and 111.0 ± 0.5° for PPy-iccm with coated particles (Class 2) (see Figure 10). This similarity can be attributed to the similar overhang structure, as described in the next section, for the various morphologies. The apparent contact angle of the bottom-surface of the sample was 62.9 ± 1.6°. This shows that the film is hydrophobic on the top-surface and hydrophilic on the bottom-surface.

As a reference, the contact angle of water on PPy grafted on a silicon wafer was measured. The average apparent contact angle for this reference PPy is 21.1 ± 1.9° (Figure 10A). Unstructured PPy has been previously found to have contact angles between 20° and 55°.[17,21,27] As our surface has micrometer-sized roughness, as is shown in the SEM image in Figure 10, the droplet is probably in a Wenzel state, and the apparent contact angle is therefore lower than the contact angle of water on a perfectly flat PPy substrate.

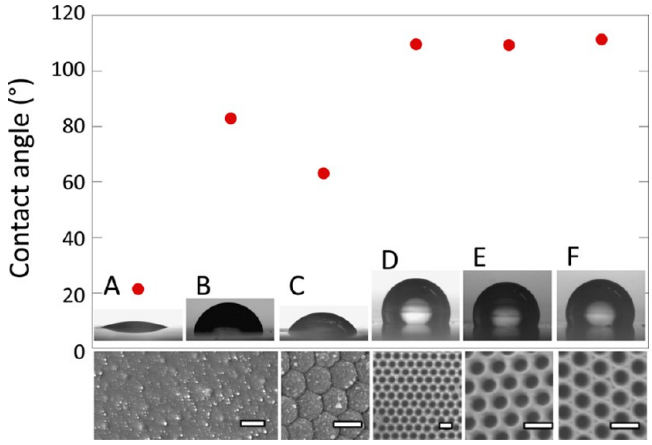

Figure 10. Contact angles of a droplet of water on PPy. (A) reference sample (PPy grafted on a silicon wafer), (B) reference sample contaminated with PS, (C) bottom of PPy-iccm, (D–F) PPy-iccms. Error bars are smaller than the symbols. Scale bars represent 10 μm for A, B and 1 μm for C–F.

Additionally, the excess C observed in the XPS measurements suggest that residual PS is left after etch removal of the template particles. As polymers tend to coat surfaces with a thin layer even at very low concentrations, and PS has a contact angle with water of 91°,[70] the effect of this residue layer on the unstructured PPy contact angle was measured. PS particles were brought into contact with unstructured PPy layer, then removed by etching in a manner similar to that used to prepare the PPy-iccms. The residue changed the apparent contact angle of the soaked PPy surface to 82.7 ± 0.7°. We attribute this change in apparent contact angle mainly to a change in interfacial tension of the solid–air interface, although polymer adsorption also subtly changes the roughness of the surface.

3.3.2. From Hydrophilic to Hydrophobic. The hydrophobic behavior of the PPy-iccms can be explained by the overhang structure of the PPy-iccm films.[31] The angle of overhang was determined by analyzing SEM micrographs of the different morphologies and was calculated to be 37° for all morphologies (see the Supporting Information for calculation details). All morphologies have the same angle of overhang, because the particles were immersed in the water to the same extent during polymerization. The immersion depth is mainly determined by the subphase, as the dissociation of –COOH groups on the surface of the particles and hence its hydrophilicity depends on the pH and ionic strength of the subphase. This also explains the fact that the contact angles for the three different morphologies of PPy-iccm are very similar.

The angle of overhang is well below the apparent contact angle of water on the PS-contaminated reference of 82.7 ± 0.7°, and hence it is possible that capillary forces act as barrier preventing water to enter the cavity.

To compare the obtained results with theory, we use the Cassie-Baxter equation (eq 2) to calculate the contact angle of water on our structures where the water cannot enter the cavities. The fraction of solid, φ_s, can be calculated in two ways: either by adding the area of all holes in the SEM image, and dividing this by the total area of the SEM image, or by assuming hexagonal packing of the particles and using the radius of the particle, R_p, and the radius of the opening of the cavities, R_h (see Supporting Information for further details). The first method underestimates φ_s because of the neglect of holes at the edge of the image and nonspherical holes, while the second method overestimates φ_s

DOI: 10.1021/acsami.5b03903
ACS Appl. Mater. Interfaces 2015, 7, 16507–16517

due to the assumption that the surface is covered with one perfect crystal lattice without defects or grain boundaries. The effective φ_s can therefore be taken as the average of these two measurements. For our samples, the first method yields a φ_s of 0.67, and the second method yields a φ_s of 0.65. Therefore, an effective φ_s of 0.66 is used for further calculations.

Using $\varphi_s = 0.66$ and $\theta_{reference} = 82.7$, we find $\theta_{air\ in\ cavity}$ of 105°. As the $\theta_{air\ in\ cavity}$ is in good agreement with the observed contact angles on the different morphologies, which are all similar, the increase in contact angle to hydrophobic behavior may be attributed to air entrapment in the cavities.

4. CONCLUSION

In summary, we introduced a scalable fabrication method to create PPy films with overhang structures yielding hydrophobic wetting behavior on a hydrophilic material. Using carboxylated PS particles at the air/water interface as template enables control over the crystallinity by choosing the pH of the subphase. By varying the monomer and oxidant concentrations, different nanopatterned surface structures can be fabricated under mild conditions. Using this approach, synthesis of surface gradients is achieved by controlling the time between adding the monomer and the oxidant. The final inverse crystalline colloidal monolayer is obtained by soaking the PPy film in THF. The apparent contact angle of water on top of the PPy-iccm is 109.5°, which indicates a switch from hydrophilic behavior for the unstructured material to hydrophobic behavior upon structuring. This can be explained by air entrapment in the cavities, because capillary forces prevent water from entering.

We have demonstrated that colloidal templating in combination with interfacial polymerization provides a promising approach to design surfaces with overhang structures. This approach is quite general and may be applied to manufacture different materials where controlled wetting behavior is required.

■ ASSOCIATED CONTENT

Supporting Information

SEM micrographs, XPS analyses, EDS analysis, and immersion depth calculations. The Supporting Information is available free of charge on the ACS Publications website at DOI: 10.1021/acsami.5b03903.

■ AUTHOR INFORMATION

Corresponding Author

*E-mail: Marleen.Kamperman@wur.nl.

Author Contributions

The manuscript was written through contributions of all authors. All authors have given approval to the final version of the manuscript.

Funding

The Netherlands Organization for Scientific Research (NWO)

Notes

The authors declare no competing financial interest.

■ ACKNOWLEDGMENTS

S.A. thanks Marcel Giesbers for his help with the EDS measurements. S.A. and M.K. acknowledge The Netherlands Organization for Scientific Research (NWO) for financial support and the Center of Advanced Technologies CAT-AgroFood for partial funding of the Scanning Auger Microscope. S.P. acknowledges NanoNextNL (program 6C) for funding.

■ ABBREVIATIONS

Py, pyrrole
PPy, polypyrrole
PPy-ccm, polypyrrole crystalline colloidal monolayers
PPy-iccm, polypyrrole inverse crystalline colloidal monolayer
PS, polystyrene

■ REFERENCES

(1) Das, T. K.; Prusty, S. Review on Conducting Polymers and Their Applications. *Polym.-Plast. Technol. Eng.* **2012**, *51* (14), 1487−1500.
(2) Forrest, S. R. The Path to Ubiquitous and Low-cost Organic Electronic Appliances on Plastic. *Nature* **2004**, *428* (6986), 911−918.
(3) Günes, S.; Neugebauer, H.; Sariciftci, N. S. Conjugated Polymer-based Organic Solar Cells. *Chem. Rev.* **2007**, *107* (4), 1324−1338.
(4) Facchetti, A. Π-conjugated Polymers for Organic Electronics and Photovoltaic Cell Applications. *Chem. Mater.* **2010**, *23* (3), 733−758.
(5) Fabretto, M. V.; Evans, D. R.; Mueller, M.; Zuber, K.; Hojati-Talemi, P.; Short, R. D.; Wallace, G. G.; Murphy, P. J. Polymeric Material with Metal-like Conductivity for Next Generation Organic Electronic Devices. *Chem. Mater.* **2012**, *24* (20), 3998−4003.
(6) Zhou, H.; Yang, L.; You, W. Rational Design of High Performance Conjugated Polymers for Organic Solar Cells. *Macromolecules* **2012**, *45* (2), 607−632.
(7) Carquigny, S.; Sanchez, J.-B.; Berger, F.; Lakard, B.; Lallemand, F. Ammonia Gas Sensor based on Electrosynthesized Polypyrrole Films. *Talanta* **2009**, *78* (1), 199−206.
(8) Hamilton, A.; Breslin, C. B. The Development of a Novel Urea Sensor using Polypyrrole. *Electrochim. Acta* **2014**, *145*, 19−26.
(9) Safarnavadeh, V.; Zare, K.; Fakhari, A. R. Capability of Parasulfonato calix[6]arene, as an Anion Dopant, and Organic Solvents in Enhancing the Sensitivity and Loading of Glucose oxidase (GOx) on Polypyrrole Film in a Biosensor: A Comparative Study. *Biosens. Bioelectron.* **2013**, *49* (0), 159−163.
(10) Apetrei, I. M.; Apetrei, C. Amperometric Biosensor based on Polypyrrole and Tyrosinase for the Detection of Tyramine in Food Samples. *Sens. Actuators, B* **2013**, *178* (0), 40−46.
(11) de Marcos, S.; Wolfbeis, O. S. Optical Sensing of pH based on Polypyrrole Films. *Anal. Chim. Acta* **1996**, *334* (1), 149−153.
(12) Koncki, R.; Wolfbeis, O. S. Composite Films of Prussian blue and N-substituted Polypyrroles: Fabrication and Application to Optical Determination of pH. *Anal. Chem.* **1998**, *70* (13), 2544−2550.
(13) Esmaeili, C.; Ghasemi, M.; Heng, L. Y.; Hassan, S. H.; Abdi, M. M.; Daud, W. R. W.; Ilbeygi, H.; Ismail, A. F. Synthesis and Application of Polypyrrole/Carrageenan Nano-bio Composite as a Cathode Catalyst in Microbial Fuel Cells. *Carbohydr. Polym.* **2014**, *114*, 253−259.
(14) Nyström, G.; Strømme, M.; Sjödin, M.; Nyholm, L. Rapid Potential Step Charging of Paper-based Polypyrrole Energy Storage Devices. *Electrochim. Acta* **2012**, *70* (0), 91−97.
(15) Feng, X.; Jiang, L. Design and Creation of Superwetting/Antiwetting Surfaces. *Adv. Mater.* **2006**, *18*, 3063−3078.
(16) Darmanin, T.; Nicolas, M.; Guittard, F. Synthesis and Properties of Perfluorinated Conjugated Polymers Based on Polyethylenedioxythiophene, Polypyrrole, and Polyfluorene. Toward Surfaces with Special Wettabilities. *Langmuir* **2008**, *24* (17), 9739−9746.
(17) Mecerreyes, D.; Alvaro, V.; Cantero, I.; Bengoetxea, M.; Calvo, P. A.; Grande, H.; Rodriguez, J.; Pomposo, J. A. Low Surface Energy Conducting Polypyrrole doped with a Fluorinated Counterion. *Adv. Mater.* **2002**, *14* (10), 749−752.
(18) Azioune, A.; Chehimi, M. M.; Miksa, B.; Basinska, T.; Slomkowski, S. Hydrophobic Protein−Polypyrrole Interactions: The Role of van der Waals and Lewis Acid−Base Forces As Determined by Contact Angle Measurements. *Langmuir* **2002**, *18* (4), 1150−1156.
(19) Chang, J. H.; Hunter, I. W. A Superhydrophobic to Superhydrophilic In Situ Wettability Switch of Microstructured Polypyrrole Surfaces. *Macromol. Rapid Commun.* **2011**, *32* (9−10), 718−723.
(20) Xu, L.; Wang, J.; Song, Y.; Jiang, L. Electrically Tunable Polypyrrole Inverse Opals with Switchable Stopband, Conductivity, and Wettability. *Chem. Mater.* **2008**, *20* (11), 3554−3556.

DOI: 10.1021/acsami.5b03903
ACS Appl. Mater. Interfaces 2015, 7, 16507−16517

(21) Kim, P.; Wong, T.-S.; Alvarenga, J.; Kreder, M. J.; Adorno-Martinez, W. E.; Aizenberg, J. Liquid-infused Nanostructured Surfaces with Extreme Anti-ice and Anti-frost Performance. *ACS Nano* **2012**, *6* (8), 6569−6577.
(22) Zhu, H.; Hou, J.; Qiu, R.; Zhao, J.; Xu, J. Perfluorinated Lubricant/ Polypyrrole Composite Material: Preparation and Corrosion Inhibition Application. *J. Appl. Polym. Sci.* **2014**, *131* (9), 40184−40192.
(23) Cao, L.; Hu, H.-H.; Gao, D. Design and Fabrication of Micro-textures for Inducing a Superhydrophobic Behavior on Hydrophilic Materials. *Langmuir* **2007**, *23* (8), 4310−4314.
(24) Bellanger, H.; Darmanin, T.; Taffin de Givenchy, E.; Guittard, F. d. r. Chemical and Physical Pathways for the Preparation of Superoleophobic Surfaces and Related Wetting Theories. *Chem. Rev.* **2014**, *114* (5), 2694−2716.
(25) Silk, T.; Hong, Q.; Tamm, J.; Compton, R. G. AFM Studies of Polypyrrole Film Surface Morphology I. The Influence of Film Thickness and Dopant Nature. *Synth. Met.* **1998**, *93* (1), 59−64.
(26) Omastová, M.; Mičušík, M. Polypyrrole Coating of Inorganic and Organic Materials by Chemical Oxidative Polymerisation. *Chem. Pap.* **2012**, *66* (5), 392−414.
(27) Acevedo, D. F.; Frontera, E.; Broglia, M. F.; Mücklich, F.; Miras, M. C.; Barbero, C. A. One Step Lithography of Polypyrrole. *Adv. Eng. Mater.* **2011**, *13* (5), 405−410.
(28) Wang, J.; Xu, Y.; Wang, J.; Du, X.; Xiao, F.; Li, J. High Charge/ Discharge Rate Polypyrrole Films Prepared by Pulse Current Polymerization. *Synth. Met.* **2010**, *160* (17), 1826−1831.
(29) Bai, Y.; Xu, Y.; Wang, J.; Gao, M.; Wang, J. Interface Effect on the Electropolymerized Polypyrrole Films with Hollow Micro/Nanohorn Arrays. *ACS Appl. Mater. Interfaces* **2014**, *6* (7), 4693−4704.
(30) Song, J.; Liu, H.; Wan, M.; Zhu, Y.; Jiang, L. Bio-inspired Isotropic and Anisotropic Wettability on a Janus Free-standing Polypyrrole Film Fabricated by Interfacial Electro-Polymerization. *J. Mater. Chem. A* **2013**, *1* (5), 1740−1744.
(31) Santos, L.; Martin, P.; Ghilane, J.; Lacaze, P. C.; Lacroix, J.-C. Micro/Nano-Structured Polypyrrole Surfaces on Oxidizable Metals as Smart Electroswitchable Coatings. *ACS Appl. Mater. Interfaces* **2013**, *5* (20), 10159−10164.
(32) Valsesia, A.; Lisboa, P.; Colpo, P.; Rossi, F. Fabrication of Polypyrrole-Based Nanoelectrode Arrays by Colloidal Lithography. *Anal. Chem.* **2006**, *78* (21), 7588−7591.
(33) Qi, G.; Huang, L.; Wang, H. Highly Conductive Free Standing Polypyrrole Films Prepared by Freezing Interfacial Polymerization. *Chem. Commun.* **2012**, *48* (66), 8246−8248.
(34) Qi, G.; Wu, Z.; Wang, H. Highly Conductive and Semitransparent Free-Standing Polypyrrole Films Prepared by Chemical Interfacial Polymerization. *J. Mater. Chem. C* **2013**, *1* (42), 7102−7110.
(35) Dallas, P.; Niarchos, D.; Vrbanic, D.; Boukos, N.; Pejovnik, S.; Trapalis, C.; Petridis, D. Interfacial Polymerization of Pyrrole and In Situ Synthesis of Polypyrrole/Silver Nanocomposites. *Polymer* **2007**, *48* (7), 2007−2013.
(36) Shinde, S. S.; Gund, G. S.; Dubal, D. P.; Jambure, S. B.; Lokhande, C. D. Morphological Modulation of Polypyrrole Thin Films through Oxidizing Agents and their Concurrent Effect on Supercapacitor Performance. *Electrochim. Acta* **2014**, *119*, 1−10.
(37) Carswell, A. D. W.; O'Rea, E. A.; Grady, B. P. Adsorbed Surfactants as Templates for the Synthesis of Morphologically Controlled Polyaniline and Polypyrrole Nanostructures on Flat Surfaces: From Spheres to Wires to Flat Films. *J. Am. Chem. Soc.* **2003**, *125* (48), 14793−14800.
(38) Wu, A.; Kolla, H.; Manohar, S. K. Chemical Synthesis of Highly Conducting Polypyrrole Nanofiber Film. *Macromolecules* **2005**, *38* (19), 7873−7875.
(39) Zhong, W.; Liu, S.; Chen, X.; Wang, Y.; Yang, W. High-Yield Synthesis of Superhydrophilic Polypyrrole Nanowire Networks. *Macromolecules* **2006**, *39* (9), 3224−3230.
(40) Lascelles, S. F.; Armes, S. P. Synthesis and Characterization of Micrometre-Sized, Polypyrrole-Coated Polystyrene Latexes. *J. Mater. Chem.* **1997**, *7* (8), 1339−1347.
(41) Cairns, D.; Armes, S.; Chehimi, M.; Perruchot, C.; Delamar, M. X-ray Photoelectron Spectroscopy Characterization of Submicrometer-Sized Polypyrrole-Polystyrene Composites. *Langmuir* **1999**, *15* (23), 8059−8066.
(42) Perruchot, C.; Chehimi, M. M.; Delamar, M.; Lascelles, S. F.; Armes, S. P. Surface Characterization of Polypyrrole-Coated Polystyrene Latex by X-ray Photoelectron Spectroscopy. *Langmuir* **1996**, *12* (13), 3245−3251.
(43) Yang, Y.; Chu, Y.; Yang, F.; Zhang, Y. Uniform Hollow Conductive Polymer Microspheres Synthesized with the Sulfonated Polystyrene Template. *Mater. Chem. Phys.* **2005**, *92* (1), 164−171.
(44) Huang, Z.; Wang, C.; Li, Y.; Wang, Z. Controlled Preparation of Core−Shell Polystyrene/Polypyrrole Nanocomposite Particles by a Swelling−Diffusion−Interfacial Polymerization Method. *Colloid Polym. Sci.* **2012**, *290* (10), 979−985.
(45) Fujii, S.; Kappl, M.; Butt, H.-J.; Sugimoto, T.; Nakamura, Y. Soft Janus Colloidal Crystal Film. *Angew. Chem., Int. Ed.* **2012**, *51* (39), 9809−9813.
(46) Wenzel, R. N. Resistance of Solid Surfaces to Wetting by Water. *Ind. Eng. Chem.* **1936**, *28* (8), 988−994.
(47) Bormashenko, E.; Bormashenko, Y.; Whyman, G.; Pogreb, R.; Stanevsky, O. Micrometrically Scaled Textured Metallic Hydrophobic Interfaces Validate the Cassie−Baxter Wetting Hypothesis. *J. Colloid Interface Sci.* **2006**, *302* (1), 308−311.
(48) Choi, H.-J.; Choo, S.; Shin, J.-H.; Kim, K.-I.; Lee, H. Fabrication of Superhydrophobic and Oleophobic Surfaces with Overhang Structure by Reverse Nanoimprint Lithography. *J. Phys. Chem. C* **2013**, *117* (46), 24354−24359.
(49) Bormashenko, E. Why does the Cassie−Baxter equation apply? *Colloids Surf., A* **2008**, *324* (1), 47−50.
(50) Cassie, A.; Baxter, S. Wettability of Porous Surfaces. *Trans. Faraday Soc.* **1944**, *40*, 546−551.
(51) Whyman, G.; Bormashenko, E. How to Make the Cassie Wetting State Stable? *Langmuir* **2011**, *27* (13), 8171−8176.
(52) Appel, J.; Akerboom, S.; Fokkink, R. G.; Sprakel, J. Facile One-Step Synthesis of Monodisperse Micron-Sized Latex Particles with Highly Carboxylated Surfaces. *Macromol. Rapid Commun.* **2013**, *34* (16), 1284−1288.
(53) Akerboom, S.; Appel, J.; Labonte, D.; Federle, W.; Sprakel, J.; Kamperman, M. Enhanced Adhesion of Bioinspired Nanopatterned Elastomers via Colloidal Surface Assembly. *J. R. Soc., Interface* **2015**, *12* (102), 20141061.
(54) Perruchot, C.; Chehimi, M.; Delamar, M.; Cabet-Deliry, E.; Miksa, B.; Slomkowski, S.; Khan, M.; Armes, S. Chemical Deposition and Characterization of Thin Polypyrrole Films on Glass Plates: Role of Organosilane Treatment. *Colloid Polym. Sci.* **2000**, *278* (12), 1139−1154.
(55) Zeng, X.; Xu, G.; Gao, Y.; An, Y. Surface Wettability of (3-Aminopropyl) triethoxysilane Self-Assembled Monolayers. *J. Phys. Chem. B* **2010**, *115* (3), 450−454.
(56) Malitesta, C.; Losito, I.; Sabbatini, L.; Zambonin, P. G. New Findings on Polypyrrole Chemical Structure by XPS Coupled to Chemical Derivatization Labelling. *J. Electron Spectrosc. Relat. Phenom.* **1995**, *76*, 629−634.
(57) Wu, Q.; Wang, Z.; Xue, G. Controlling the Structure and Morphology of Monodisperse Polystyrene/Polyaniline Composite Particles. *Adv. Funct. Mater.* **2007**, *17* (11), 1784−1789.
(58) Yang, M.; Cao, L.; Tan, L. Synthesis of Sea Urchin-Like Polystyrene/Polyaniline Microspheres by Seeded Swelling Polymerization and their Catalytic Application. *Colloids Surf., A* **2014**, *441*, 678−684.
(59) Lee, J. M.; Lee, D. G.; Lee, S. J.; Kim, J. H.; Cheong, I. W. One-Step Synthetic Route for Conducting Core− Shell Poly (styrene/ pyrrole) Nanoparticles. *Macromolecules* **2009**, *42* (13), 4511−4519.
(60) Tan, Y.; Ghandi, K. Kinetics and Mechanism of Pyrrole Chemical Polymerization. *Synth. Met.* **2013**, *175*, 183−191.
(61) Planche, M.; Thieblemont, J.; Mazars, N.; Bidan, G. Kinetic Study of Pyrrole Polymerization with Iron (III) chloride in Water. *J. Appl. Polym. Sci.* **1994**, *52* (13), 1867−1877.

DOI: 10.1021/acsami.5b03903
ACS Appl. Mater. Interfaces 2015, 7, 16507−16517

(62) Armes, S. P. Optimum Reaction Conditions for the Polymerization of Pyrrole by Iron (III) chloride in Aqueous Solution. *Synth. Met.* **1987**, *20* (3), 365−371.
(63) Satoh, M.; Kaneto, K.; Yoshino, K. Dependences of Electrical and Mechanical Properties of Conducting Polypyrrole Films on Conditions of Electrochemical Polymerization in an Aqueous Medium. *Synth. Met.* **1986**, *14* (4), 289−296.
(64) Palmisano, F.; Malitesta, C.; Centonze, D.; Zambonin, P. Correlation Between Permselectivity and Chemical Structure of Overoxidized Polypyrrole Membranes used in Electroproduced Enzyme Biosensors. *Anal. Chem.* **1995**, *67* (13), 2207−2211.
(65) Kang, E.; Neoh, K.; Ong, Y.; Tan, K.; Tan, B. X-ray Photoelectron Spectroscopic Studies of Polypyrrole Synthesized with Oxidative Iron (III) Salts. *Macromolecules* **1991**, *24* (10), 2822−2828.
(66) Taşdelen, B.; Kayaman-Apohan, N.; Güven, O.; Baysal, B. M. Preparation of Poly (N-isopropylacrylamide/itaconic acid) Copolymeric Hydrogels and their Drug Release Behavior. *Int. J. Pharm.* **2004**, *278* (2), 343−351.
(67) Vogel, N.; Weiss, C. K.; Landfester, K. From Soft to Hard: the Generation of Functional and Complex Colloidal Monolayers for Nanolithography. *Soft Matter* **2012**, *8* (15), 4044−4061.
(68) Machida, S.; Miyata, S.; Techagumpuch, A. Chemical Synthesis of Highly Electrically Conductive Polypyrrole. *Synth. Met.* **1989**, *31* (3), 311−318.
(69) Chougule, M.; Pawar, S.; Godse, P.; Mulik, R.; Sen, S.; Patil, V. Synthesis and Characterization of Polypyrrole (PPy) Thin Films. *Soft Nanosci. Lett.* **2011**, *1* (1), 6−10.
(70) Owens, D. K.; Wendt, R. C. Estimation of the Surface Free Energy of Polymers. *J. Appl. Polym. Sci.* **1969**, *13* (8), 1741−1747.

DOI: 10.1021/acsami.5b03903
ACS Appl. Mater. Interfaces 2015, 7, 16507−16517